Open cavity receiver geometry influence on radiative losses

Charles-Alexis Asselineau [1], Ehsan Abbasi [1], John Pye [1]
[1] Solar Thermal Group, College of Engineering and Computer Science (CECS), Australian National University (ANU), Canberra, ACT 0200 Australia.
Email address: charles-alexis.asselineau@anu.edu.au

Keywords: Receiver design, Radiative transfer, Ray tracing.

Abstract

Open cavity receivers can be used to efficiently absorb concentrated solar radiation at high temperatures. Using ray-tracing and a stochastic optimisation method, the geometry of such receivers is optimised looking at radiative losses only. Results confirm the major role of the aperture in cavity losses mitigation and highlight the flux distribution variation on geometries with comparable radiative performances.

1 - Open cavity receivers losses in concentrated solar applications.

In Concentrated Solar Power (CSP) systems, the receiver, placed at the focus of the light-concentrator, absorbs concentrated solar radiation and transfers this heat to a Heat Carrier (HC). Recent advances in CSP applications target higher temperatures of operation for receivers in order to increase the thermodynamic efficiency of the overall CSP system. In the present study, the geometry of cavity receivers is analysed using a stochastic brute force optimisation technique.

Open cavity receivers act as virtual black bodies, trapping light through multiple reflections in order to increase the amount energy absorbed. These receivers are subject to 3 general types of losses that have to be minimized:

- Radiative losses due to optical behaviour and thermal emissions.
- Convective losses to the surroundings due to difference of air temperatures in the cavity enclosure and the environment.
- Losses through the walls of the receiver mostly driven by heat conduction.

Convective losses, not considered here, are hard to model with confidence due to the difficulty in validating the results of simulations and correlations used [1]. Losses through the walls by heat conduction, driven by the conditions of concentrated solar radiation on the internal walls of the cavity and insulation material chosen are neglected in this study.

The cavity receiver of choice is assumed to be composed of grey-body behaving internal surfaces. Radiative losses, as labelled in this study, are regrouping the optical losses due to non-ideal concentration of the incoming solar radiation as well as thermal emission losses described by the Stefan-Boltzmann law. Although the influence of the aperture on the radiative efficiency of cavity receivers is generally understood, the rest of the cavity geometry is usually not analysed in detail. The overall first-law efficiency of cavity receivers is reported to be fairly independent of the geometrical design chosen, provided that the aperture of the cavity is carefully chosen and the internal area over aperture area ratio is high enough to provoke a significant “cavity effect” [2].

Notations:

ra	Aperture radius	m
rc	Cone radius	m
lf	Frustum length	m
lc	Cone length	m
q	Radiative flux	W
J	Radiosity	W
T	Temperature	K
A	Area	m^2
n	Number of discrete elements on the receiver internal wall	1
N	Number of rays in the raytrace considered	1
ε	Emissivity	1
σ	Stefan-Boltzman constant	$W.m^{-2}.K^{-4}$
$F_{i->j}$	View factor of element I looking at j	1

Actually, the geometry has a strong influence on the heat flux distribution on the absorbing walls of the cavity [3]. When looking at high temperatures of operations (>650°C), sharp variations of heat flux distribution and hot spots can be challenging when looking at materials stability and thermal-cycling induced fatigue. Shuai et al. 2008 [4] propose a semi-analytical procedure to optimise open cavity geometries in order to homogenise the internal flux distribution. Their method is based on a first stage of Monte-Carlo ray-tracing to obtain the focal plane flux distribution and a second stage where they analytically derive the radiative flux on the internal walls from specific locations on this aperture plane. Considering black surfaces and diffuse reflections as well as no thermal emissions, they run an algorithm to progressively optimise a faceted geometry in order to get the most homogeneous flux distribution on the internal walls of the cavity. The present study is adopting a different approach:

- The objective is to maximise the heat that can be extracted by the receiver.
- Simple model for the cavity geometry using a set of 4 parameters.
- Ray-trace simulation of the entire scene including reflections in the receiver.
- Thermal emissions are taken into account.
- Stochastic approach in geometries declaration and optimisation.

2 – Case study: Big Dish saturated steam generation with a parametric cavity.

For this study, the example of a parabolic dish concentrator system is considered. The dimensions of the simulated parabolic dish are approximately the ones of the Big Dish at ANU [5], composed of 380 spherically curved square mirror panels deflected to a parabolic frame. Parasitic absorption of solar radiation due to non ideal reflectivity of the mirrors and concentrator shape error due to non-ideal orientation of the reflective surface and parabolic approximation of the Big Dish are considered [6]. Concentrator surface slope error is modeled using a Gaussian bi-variate distribution of standard deviation of the normal to the surface [7].

Diameter	22 m
Focal length	13.4 m
Reflectivity	0.94
Shape error	4 mrad

Table 1: Geometrical and optical properties of the Big Dish.

The open cavity receiver, placed at the focus of the parabolic dish, is an axisymmetric receiver defined by four geometric parameters: aperture radius r_a, cone

radius r_c, frustum depth l_f and cone depth l_c. As shown in Figure 1, the combination of these four parameters is able to create a wide variety of geometries. Cavity walls are considered to be grey (uniform spectral emissivity) and diffuse which are common assumptions for many oxidised surfaces. The emissivity ε is set to 0.87[8].

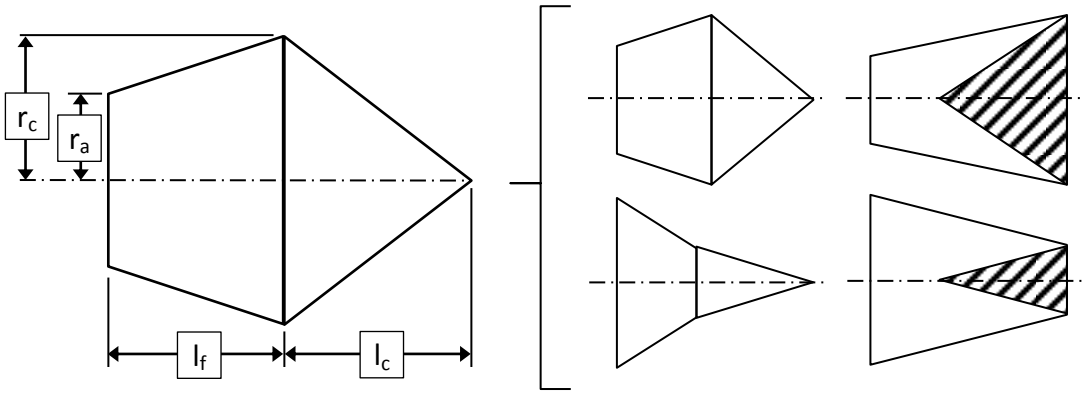

Figure 1: 4 parameter cavity receiver diagram and examples of geometries.

3 – Radiative losses study.

3.1 – Receiver optical loss simulation

The optical behaviour of the system is simulated using the Monte-Carlo ray-tracing method [9]. The specific code used is "Tracer" by Y. Meller, an open-source ray-tracing code written in python (https://github.com/yosefm/tracer).

The light source declared in the present ray-tracing procedure is a disc which radius is sufficient to encompass the full scene and oriented so that its normal vector is collinear with the zenith vector of the scene. Rays' starting positions are randomly declared on the surface of this disc. Rays' directions and energy transported are determined according to the Buie sunshape model [10]. The Buie sunshape correlates the angular intensity distribution of solar radiation with a circumsolar ratio (CSR) parameter. The CSR is is a function only of local atmospheric conditions such as humidity and dust content and quantifies the "spread" of directly incoming sunlight due to atmospheric interactions. In this work we use a Buie sunshape with CSR=0.2 meaning that 20% of the incoming radiation flux comes from the aureole region around the solar disc.

Source radius	13.2 m
Solar disc half-angle	4.65 mrad
Direct Normal Irradiance (DNI)	1000 W/m^2

Table 2: Light source properties.

A ray tracking algorithm is implemented in order to keep track of the amount of optical losses and their breakdown. Optical losses are subdivided into 4 categories to account for the 4 major optical losses sources impacting receiver designs.

- Blockage losses: Some rays are not reaching the concentrator surfaces due to the presence of the receiver on their way.
- Parasitic absorption by the concentrator: Concentrator mirrors do not have an ideal reflectivity of 1. Some energy is absorbed by the surface of the mirror when the ray is reflected.

- Spillage losses: Rays escaping the source have a certain angular deviation compared to the optimal trajectory. Several effects, taken into account in the sunshape model used for the source, cause this deviation. Additionally, the mirrors of the concentrator do not have a perfect shape either. As a consequence to these combined effects, some rays to miss the receiver aperture after being reflected.
- Reflective losses: Some of the energy transported by rays leaves the cavity before being fully absorbed and is lost for the system.

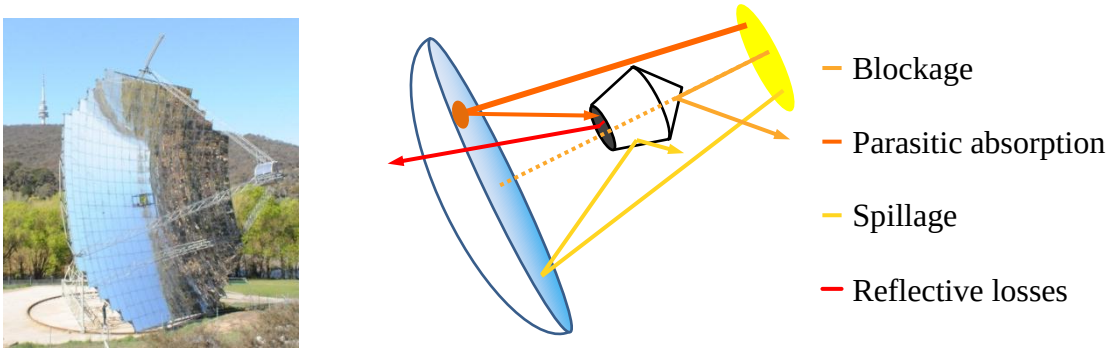

Figure 2: The Big Dish at the ANU STG facilities (left) and optical losses breakdown diagram (right).

The 3D coordinates set and associated energy loss of each ray/surface intersection are also recorded in order to be able to analyse flux distributions. Specular reflections follow a Snell-Descartes law of reflection. If the intercepted surface presents a shape error, its local normal is modified according to the Gaussian bi-variate standard deviation components and the calculation of the direction of the reflected ray is performed. Diffusely reflective surfaces are approximated by setting random reflected ray directions according to a uniform probability law.

3.2 – Thermal emission losses calculation

Thermal emissions are calculated using the radiosity problem formulation applied to diffuse grey bodies. The following system of linear equations describes the radiosity formulation for such problems [11]:

$$\begin{bmatrix} 1+(1-\varepsilon_1)F_{1\to1} & \cdots & -(1-\varepsilon_1)F_{1\to n} \\ \vdots & \ddots & \vdots \\ -(1-\varepsilon_n)F_{n\to1} & \cdots & 1+(1-\varepsilon_n)F_{n\to n} \end{bmatrix} \begin{bmatrix} J_1 \\ \vdots \\ J_n \end{bmatrix} = \begin{bmatrix} \varepsilon_1\sigma T_1^4 \\ \vdots \\ \varepsilon_n\sigma T_n^4 \end{bmatrix} \quad (1)$$

This is solved by a matrix inversion routine using LU decomposition scheme with partial pivoting and row interchanges. In order to compute thermal emissions, the view factor coefficients $F_{i->j}$, describing the geometrical interactions in the scene, have to be determined. This is done using a ray-tracing view factor calculation routine. The cavity receiver profile is discretised into *n* elements that are successively considered as sources. The view factors of each surface element to all the surface elements of the scene are determined by accounting hits. The precision of the view factor calculation routine is controlled through standard deviation evaluation and view factors reciprocity theorem validation. The present model does not consider the extraction of the heat absorbed at the internal walls of the cavity by the heat transfer fluid. As a consequence, a temperature boundary condition must be set at the wall location in order to be able to perform a thermal emission loss

calculation. A constant temperature of 650°C is on the receiver internal walls and an ambient temperature of 20°C is imposed on the aperture.

3.3 – Simulation procedure.

A brute-force optimization approach is adopted in this paper: 1000 different geometries of cavities corresponding to 1000 sets of 4 parameters are simulated and compared. Geometries are randomly declared within the parameter ranges with a uniform probability distribution. A “bounding box” philosophy is adopted to determine the parameters boundaries: all geometries have to fit in a cylinder of 3m radius by 3m length. Due to numerical constraints on floating point rounding, a lower boundary must be set on the cone radius parameter. The aperture role in spillage and thermal emissions being understood [12], a first low-precision simulation was performed in order to restrict the aperture radius range to values close to the optimum. Table 3 summarises the parameter ranges adopted for this study.

Aperture radius (m)	$0.3 < r_a < 0.6$
Cone radius (m)	$0.05 < r_c < 3$
Frustum depth (m)	$0 < l_f < 3$
Cone depth (m)	$-3 < l_c < 3$

Table 3: 4 parameters simulation range.

The number of rays used for each simulation influences the accuracy of the result. The ray-tracing method employed in this study is an explicit procedure: all rays are declared and computed simultaneously at each step of the ray-trace. This is made possible by use of the powerful numerical computing libraries available in Python and NumPy and a moderate number of rays for each geometry (1,000,000).

In order to mitigate this uncertainty, a set of 5 reference geometries belonging to the parameter domain considered was established and comprehensively evaluated. Each of these geometries was selected so as to verify the good behaviour of the model:

- A: Smallest area configuration
- B: Thin and long concave cone and flat aperture plane.
- C: Average geometry
- D: Cone dominant geometry
- E: Highest area with convex cone

	r_a (m)	r_c (m)	l_f (m)	l_c (m)
A	0.3	0.05	0.01	0.01
B	0.3	0.05	0.01	2.99
C	0.4	1.5	1.5	1.5
D	0.5	1.5	0.01	2.99
E	0.6	3	3	-2.99

Table4: Test-geometries used in ray-trace confidence interval analysis.

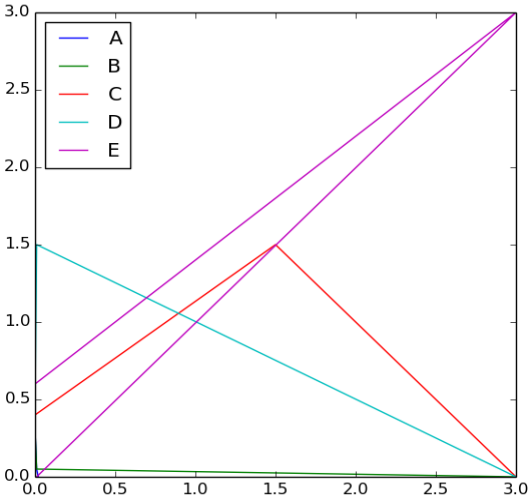

Figure 3: Reference-geometries profiles.

All five reference geometries were simulated 50,000 times with 1,000 rays each time in order to get an estimation of evolution of the precision of the results from 1,000 rays to 50,000,000 rays. Figure 4 presents the evolution of the confidence

interval on the net radiative flux, considering radiative losses and thermal emissions, for the five test geometries mentioned. The probability distribution of radiative losses for all geometries being approximately Gaussian, the three sigma rule applied to normal law probability distributions can be used to compute the tolerance interval of the raytrace results (IC=±3σ) with a known 99.7% of confidence level. Table 5 presents the values for these rounded confidence intervals relatively to the number of rays used.

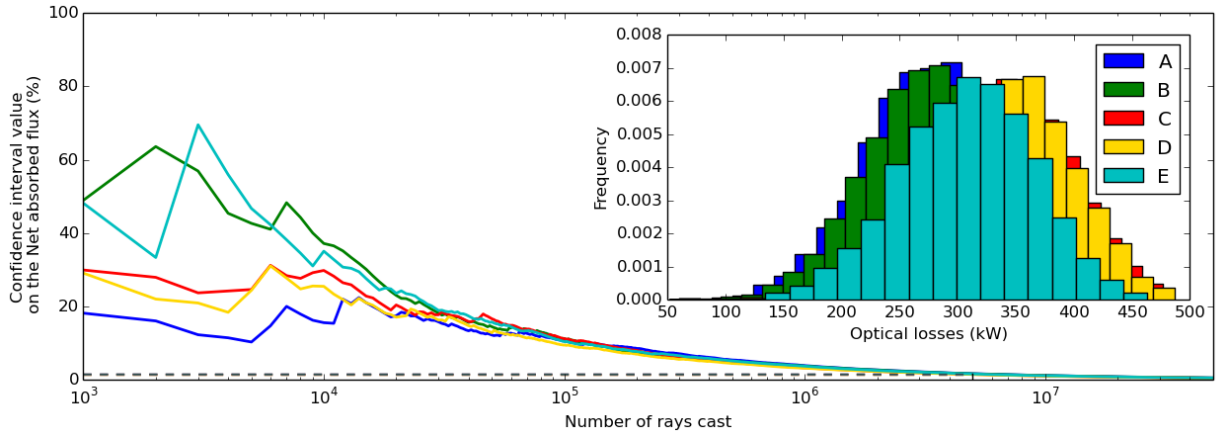

Figure 4: Raytrace precision evaluation with 5 test-cases.

	Overall radiative losses simulation confidence interval (%)									
Rays	$1x10^6$	$2x10^6$	$3x10^6$	$4x10^6$	$5x10^6$	$10x10^6$	$15x10^6$	$20x10^6$	$30x10^6$	$40x10^6$
A	3.88	2.72	2.20	1.88	1.68	1.18	0.95	0.83	0.68	0.59
B	3.76	2.68	2.15	1.86	1.66	1.18	0.96	0.83	0.68	0.59
C	3.28	2.33	1.92	1.68	1.50	1.07	0.87	0.75	0.62	0.54
D	3.20	2.28	1.89	1.65	1.47	1.04	0.85	0.74	0.60	0.52
E	3.71	2.57	2.08	1.80	1.61	1.13	0.92	0.80	0.66	0.57
IC	**3.9**	**2.8**	**2.3**	**1.9**	**1.7**	**1.2**	**1.0**	**0.9**	**0.7**	**0.6**

Table 5: Radiative losses simulation confidence intervals estimation.

Assuming that the five reference geometries are able to describe coherently the behaviour of the model on the overall parameter space at a each given number of rays, the confidence interval value given in the last row is chosen as an acceptable value for all geometries at this number of rays. All simulations were performed on a Intel Core i7-3770 CPU at 3.40GHz frequency using 7.7GiB of 1600 MHz DDR3. Evaluation of the 1,000 geometries including radiosity and ray-tracing required approximately 30 hours of processor houses on a single CPU core.

4 – Efficient geometries and results interpretation.

4.1 – Optimum geometry identification

Figure 5 shows the scatter of net absorbed fluxes, defined as the energy absorbed by the internal cavity wall subtracted from thermal emissions, plotted against each of the four geometrical parameters selected after a first ray-trace with 1,000,000 rays for each of the 1,000 geometries considered.

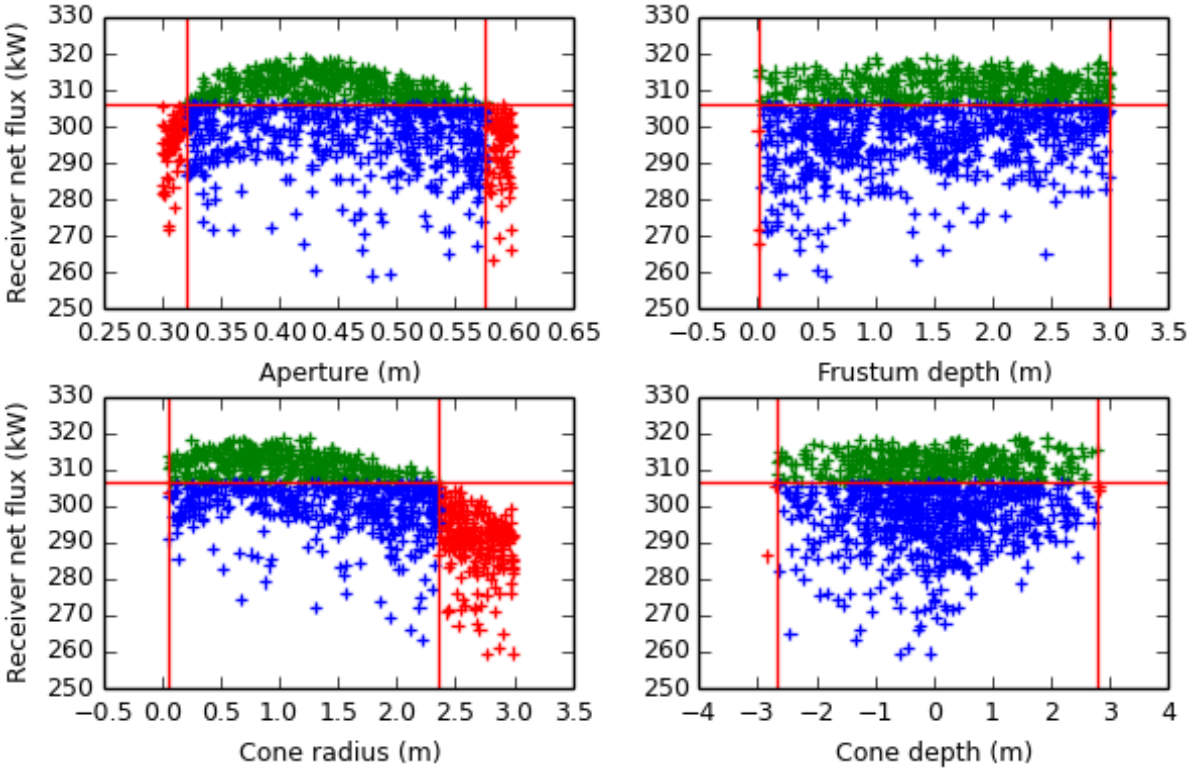

Figure 5: Net absorbed flux at the absorbing walls location in function of the 4 parameters with 1,000,000 rays.

The horizontal line, located at $y = q_{max}(1 - IC)$, accounts for the 6σ limit below which the net absorbed flux is lower than the maximum identified, with 99.7% confidence level. All geometries whose net absorbed flux is below this red line are almost certainly underperforming. General trends in Figure 5 indicate the existence of optimal aperture and cone radii. Frustum and cone depth influence on the net absorbed flux cannot be interpreted from these plots.

In Figure 6, the breakdown of radiative losses for each geometry as a function of the aperture confirms the clear influence of the aperture radius on spillage losses and thermal emissions.

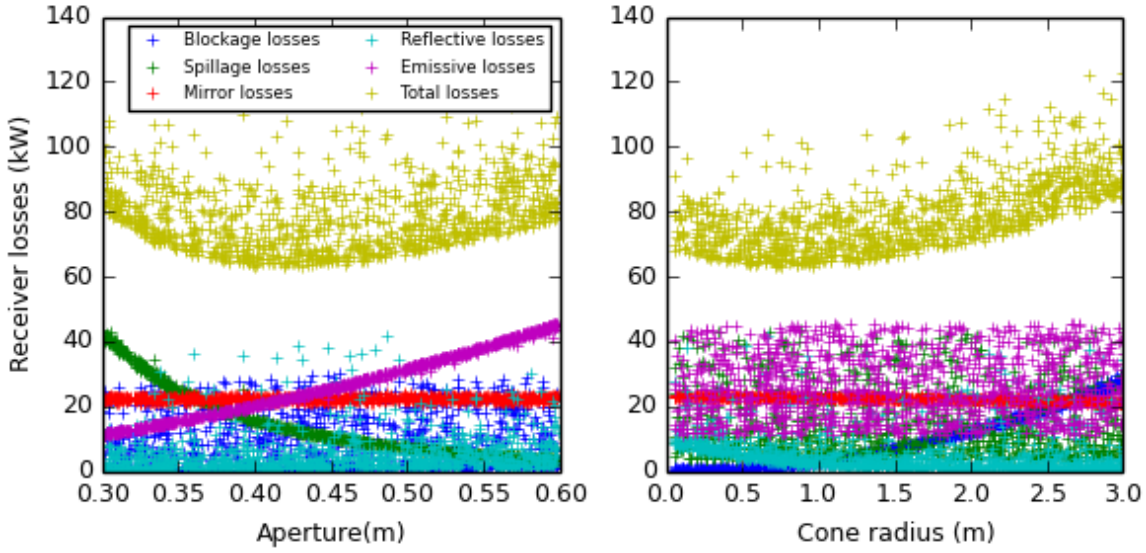

Figure 6: Radiative loss breakdown in function of the aperture radius (left) and cone radius (right).

As expected, mirror absorption losses are not a function of receiver geometry. The trade-off between increasing the aperture radius to accept more concentrated radiation in the cavity and reducing the aperture to lower the view factor to the outside and consequently reduce the thermal emissions is well illustrated here. Radiative losses breakdown in function of the cone radius plotted in Figure 6 highlight the direct correlation between the cone radius and blockage losses. The cone radius, when greater than the aperture radius, increases the area of the receiver's projected shadow on the concentrator, thus reducing the amount of concentrated radiation that will reach the aperture after hitting the collector area.

As shown in Figure 5, 1,000,000 rays are not sufficient to identify an optimum. The precision of the results is increased by performing new simulations adding progressively more rays to the interesting candidates so as to differentiate them from the under-performing geometries. Confidence intervals for higher number of rays were presented in Table 5. Figure 7 presents the algorithm used to select the best candidates from among all simulated geometries. As a result of this optimisation routine, only well-performing geometries are passed on to the next step to be simulated again. It offers a consequent gain in computation time making it possible to reduce the number of candidates from 1,000 to 26 with known precision.

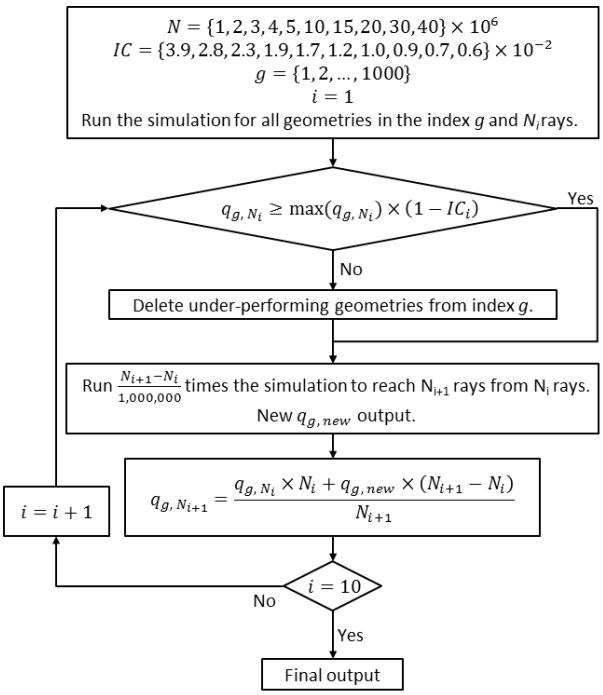

Figure 7: Stochastic optimisation algorithm diagram.

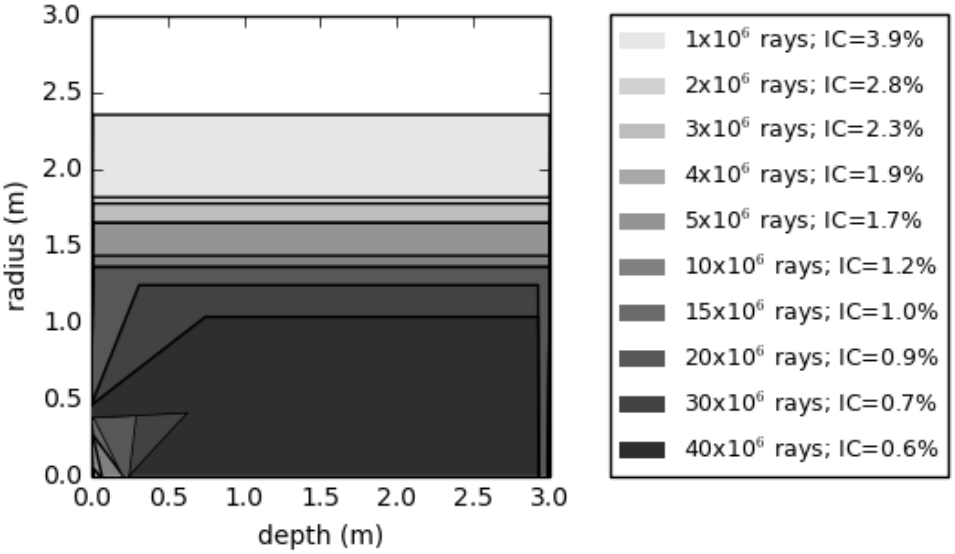

Figure 8: Evolution of the geometrical parameter space during the optimisation.

Figure 8 shows the evolution of the parameter space, accounting for all geometrical possibilities between the maximum and minimum values of each of the four geometrical parameters at each iteration. Starting from the full parameter space

chosen as boundary for the first 1,000 geometries and progressively shriking to a smaller domain after 10 iterations. For this study, the stochastic algorithm ran up to 40,000,000 rays precision. At this stage, all remaining 26 geometries share comparable performance levels within a confidence interval 0.60% (still with 99.7% confidence level), making it uncertain to choose a best candidate.

4.2– Analysis of optimal receiver geometry.

The 26 geometries identified as potential optima are divided into 2 groups: the convex cone group with $l_c < 0$ and the concave cone group with $l_c > 0$. In each group we present the flux and flux density distributions for the cases with smallest and largest internal surface area. New view factor matrixes with 100 surface elements (50 for the frustum part and 50 for the cone part) were calculated and new simulations with 40,000,000 rays were performed in order to obtain the flux distributions in Figure 9.

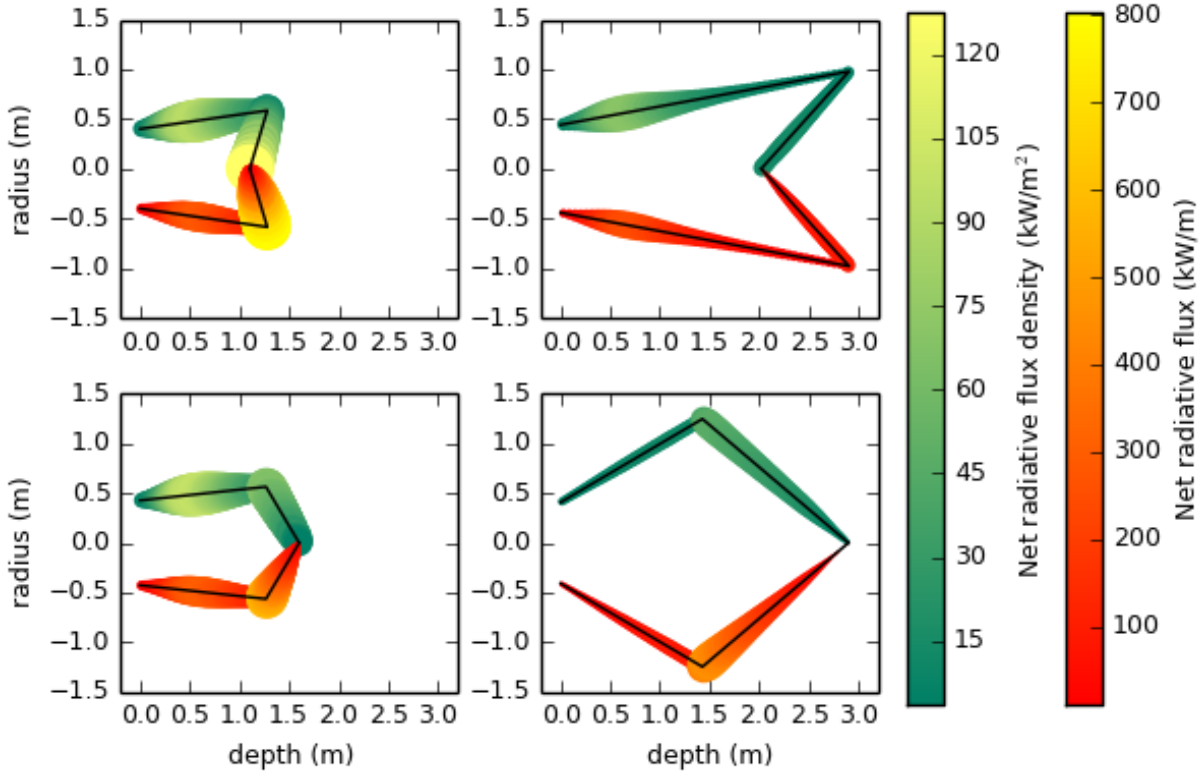

Figure 9: Axis-symmetrical profiles of identified cases and their resulting net radiative flux density (upper part of the profile) and net radiative flux (lower part of the profile).

Although these four geometries share very similar radiative efficiencies, their flux and flux density distributions are relatively different. Receivers with larger area show lower peak flux densities. Flux densities on the bottom of the optimal cavities are strongly influenced by the convex or concave nature of the conical part. In the bottom right case, most of the incoming concentrated radiation reaches the bottom cone due to a larger frustum half-angle.

5 – Conclusion

The four parameter open cavity receiver is analysed using a stochastic optimisation technique. Radiative losses are found mainly depending on the aperture

radius and cone radius due to thermal emissions and blockage losses influence. The optimisation conducted does not favour concave or convex geometries for cavities considering radiative efficiency solely. Flux distributions, highly depending on the cavity geometry, differ greatly for geometries with very similar radiative efficiencies. Radiative efficiency alone does not define an optimal shape for cavity receivers. In further work, coupling the present radiative model with temperature profiles caused by heat extraction and convective losses will give more information on the efficiency of the geometries identified.

Acknowledgements

This project has been supported by the Australian Government through the Australian Solar Institute (ASI)). The Australian Government, through ASI, is supporting Australian research and development in solar photovoltaic and solar thermal technologies to help solar power become cost competitive with other energy sources.

References

[1] Paitoonsurikarn S, Hughes G, Pye J, Lovegrove K. Numerical investigation of natural convection loss from cavity receivers in Solar Dish Applications; 2011. Available from: http://dx.doi.org/-10.1115/1.4003582.

[2] Harris JA, Lenz TG. Thermal performance of solar concentrator/cavity receiver systems. Solar Energy. 1985;34(2):135 – 142. Available from: http://www.sciencedirect.com/science/article/pii/-0038092X85901707.

[3] Hathaway BJ, Lipinski W, Davidson JH. Heat Transfer in a Solar Cavity Receiver: Design Considerations. Numerical Heat Transfer, Part A: Applications. 2012;62(5):445–461. Ávailable from: http://www.tandfonline.com/doi/abs/10.1080/10407782.2012.703471.

[4] Shuai Y, Xia XL, Tan HP. Radiation performance of dish solar concentrator/cavity receiver systems. Solar Energy. 2008;82(1):13 – 21. Available from: http://www.sciencedirect.com/-science/article/pii/S0038092X07001235.

[5] Lovegrove K, Burgess G, Pye J. A new 500m^2 paraboloidal dish solar concentrator. Solar Energy. 2011;85(4):620 – 626. SolarPACES 2009. Available from: http://-www.sciencedirect.com/science/article/pii/S0038092X10000228.

[6] Burgess G, Scott P, Pye J. Spherical and asymmetric mirror panels for paraboloidal concntrators. In: ISIS-AP - 3rd International Solar Energy Society Conference - Asia Pacific region (ISES-AP-08) Incorporating the 46th ANZES Conference. Sydney Convention & Exhibition Center; 2008. .

[7] Huang W, Han Z. Theoretical analysis of error transfer from the surface slope to the reflected ray and their application in the solar concentrated collector. Solar Energy. 2012;86(9):2592 – 2599. Available from: http://www.sciencedirect.com/science/article/pii/S0038092X12002071.

[8] Ho CK, Mahoney AR, Ambrosini A, Bencomo M, Hall A, Lambert TN. Characterization of Pyromark 2500 Paint for High-Temperature Solar Receivers. Journal of Solar Energy Engineering. 2013 Jul;136(1):014502–014502. Available from: http://dx.doi.org/10.1115/-1.4024031.

[9] Modest MF. Radiative Heat Transfer. Elsevier, editor. Academic Press; 2003.

[10] Buie D, Monger AG, Dey CJ. Sunshape distributions for terrestrial solar simulations. Solar Energy. 2003;74(2):113 – 122. Available from: http://www.sciencedirect.com/science/article/pii/-S0038092X03001257.

[11] Incropera FP, Dewitt DP. Fundamentals of Heat and Mass Transfer. 6th ed. Sons JW, editor. John Wiley & Sons; 2006.

[12] Steinfeld A, Schubnell M. Optimum aperture size and operating temperature of a solar cavity-receiver. Solar Energy. 1993;50(1):19 – 25. Available from: http://www.sciencedirect.com/-science/article/pii/0038092X93900048.